Progress In Electromagnetics Research, PIER 15, 165–189, 1997

A HYBRID INTEGRAL AND DIFFERENTIAL EQUATION METHOD SOLUTION OF SCATTERING OF TM EXCITATION BY BURIED INHOMOGENEOUS CYLINDERS

X.-B. Xu and J. Ao

1. Introduction
2. Formulation of Integral and Differential Equations
3. Hybrid FEM/MOM Numerical Solution
4. Far-Zone Scattered Field and Field Inside the Cylinder
5. Results and Discussion
References

1. Introduction

The prediction of electromagnetic scattering from buried objects has many applications in areas such as detection of tunnels, pipes, and mines, as well as exploration of mineral deposits. For decades, a lot of work was done in this area [1–7]. Recently, surface integral equation methods have been employed to determine the scattering by PEC cylinders near a planar media interface [8–14]. More recently, the investigation of scattering and radiation by a three-dimensional PEC object of arbitrary shape located in layered media has been completed by employing mixed potential integral equations [15,16]. In addition to a PEC object, surface integral equation methods have also been used to treat a buried homogeneous dielectric cylinder [17,18]. Both the frequency domain solution and the time domain response are obtained in [19]. In contrast to the work listed above, volume integral equation methods have been used for determining the scattering by a buried lossy dielectric cylinder [19]. Most recently, a hybrid surface and volume

integral equation method (HIE) has been developed and employed for the analysis of scattering by an inhomogeneous cylinder located in an infinite homogeneous space [20], and by an inhomogeneous cylinder buried below a planar media interface [21–23].

Alternative to the integral equation methods mentioned above, a number of hybrid numerical techniques have been developed for the analysis of inhomogeneous scatters located in an infinite homogeneous space – a space without media interface [24]. The unimoment method presented in [24] is suitable for treating an inhomogeneous circular cylinder. Researchers have also presented a hybrid finite element and moment (FEM/MOM) method, retaining efficient characteristics of both methods, for determining electromagnetic scattering from inhomogeneous objects, again, located in an infinite homogeneous space [25–29].

In this paper, we employ the hybrid FEM/MOM method presented by Yuan et al. [25] to analyze the scattering by an inhomogeneous lossy dielectric/ferrite cylinder buried below a planar interface between two half-spaces of different electromagnetic properties. A cross sectional view of the cylinder and the half spaces are illustrated in Fig. 1. The electromagnetic parameters are μ_a, ε_a for region a and μ_b, ε_b for region b, where ε_b, and/or μ_b may be complex to represent losses in region b. The cylinder is characterized by (μ_c, ε_c) where μ_c and/or ε_c may be complex, and they may be continuous or discrete functions of position (x, y). The cylinder is of general cross section, infinite extent, and its axis is parallel to the interface. The excitation is time harmonic, transverse magnetic (TM) and invariant with respect to the cylinder axis (z-axis). In the formulation of the integral equation part of the hybrid formulation, Sommerfeld integrals [30] are included to take into account the effect of the media interface. Also, the weak form of the wave equation is formulated in a general way such that it is suitable for the analysis of a buried cylinder with either continuous or discontinuous permeability. Comparing the hybrid FEM/MOM method with the HIE method [21–23], it is simpler to be implemented to treat a buried cylinder which has a discrete media parameter distribution. Even though the HIE method, as an integral equation method, can be employed to handle this kind of problem [23], the numerical solution procedure becomes inefficient when there are a number of regions of discontinuous electromagnetic parameters within the cylinder. But since the FEM part of the hybrid FEM/MOM method is a dif-

ferential equation solution technique, this method is most suitable for treating any kind of inhomogeneous objects, including the ones with discontinuous parameters. The method presented in this paper can be extended to the case that the excitation is transverse electric (TE) to the cylinder axis, which is the dual of the case analyzed in this paper.

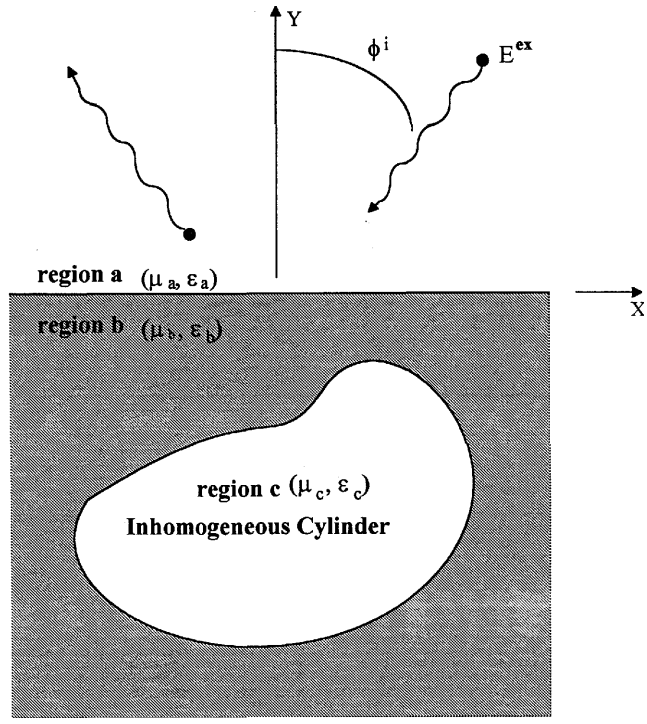

Figure 1. Inhomogeneous cylinder located below a planar media interface and illuminated by a known source.

2. Formulation of Integral and Differential Equations

As the first step of the formulation of the hybrid integral and differential equations, the equivalence principle [31] is used to construct the equivalent models of the original problem which is described in Fig. 2(a). The equivalent model which is valid in the region external to the cylinder (regions a and b) is shown in Fig. 2(b), where the cylinder is replaced by the medium surrounding it and an equivalent electric surface

current $\vec{J}$ is placed on the surface of the cylinder. Once the equivalent current $\vec{J}$ is determined, the scattered fields can be computed based on knowledge of the current. Fig. 2(c) depicts the equivalent model for the interior region of the cylinder (region c). In this figure, $\vec{H}_t$ denotes the tangential magnetic field on the cylinder surface S. The fields in the interior region of the cylinder can be uniquely determined by $\vec{H}_t$.

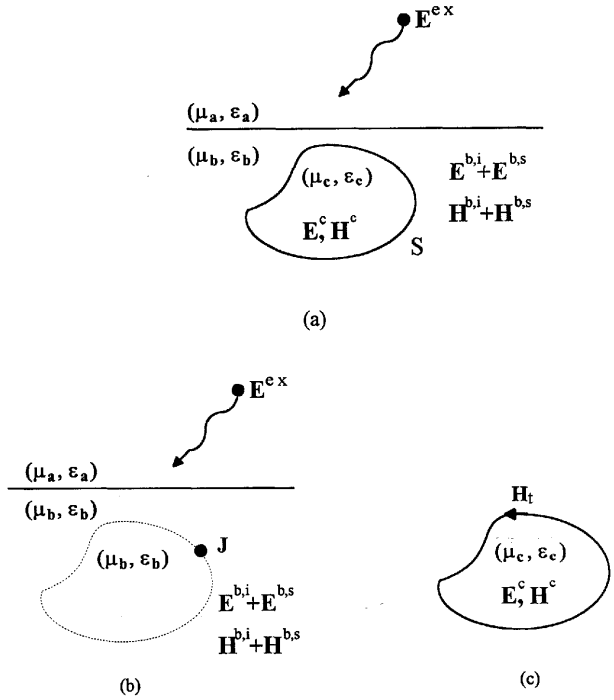

Figure 2. Equivalent models of an inhomogeneous cylinder under TM illumination. (a) Original problem; (b) Exterior equivalence; (c) Interior equivalence.

Using the equivalent model displayed in Fig. 2(b), we can express the electric and magnetic field in region b as

$$\vec{E}^b = \vec{E}^{b,i} + \vec{E}^{b,s}(\vec{J}), \tag{1}$$

and

$$\vec{H}^b = \vec{H}^{b,i} + \vec{H}^{b,s}(\vec{J}). \tag{2}$$

In Eqs. (1) and (2), ($\vec{E}^{b,i}, \vec{H}^{b,i}$) are the incident electromagnetic fields caused by a known source, observed in the absence of the cylinder. The

scattered fields ($\vec{E}^{b,s}, \vec{H}^{b,s}$) are the fields produced by the equivalent electric surface current $\vec{J}$ radiating in the presence of the planar interface of the two semi-infinite half spaces. Meanwhile, using the interior equivalence model, we may express the electric and magnetic field in region c as functions of the tangential magnetic field $\vec{H}_t$,

$$\vec{E}^c = \vec{E}^c(\vec{H}_t), \tag{3}$$

and

$$\vec{H}^c = \vec{H}^c(\vec{H}_t). \tag{4}$$

By enforcing the continuity of the tangential components of the electric and magnetic field on the surface of the inhomogeneous cylinder, we arrive at

$$\hat{n} \times \vec{E}^{b,s}(\vec{J}) - \hat{n} \times \vec{E}^c(\vec{H}_t) = -\hat{n} \times \vec{E}^{b,i}, \qquad \text{on } S, \tag{5}$$

and

$$\hat{n} \times \vec{H}^{b,s}(\vec{J}) - \vec{H}_t = -\hat{n} \times \vec{H}^{b,i}, \qquad \text{on } S, \tag{6}$$

in which $\hat{n}$ is the unit vector normal to S, pointing outward from region b . For an infinitely long cylinder under TM illumination, Equations (5) and (6) can be rewritten as

$$E_z^{b,s}(J_z) - E_z^c(H_l) = -E_z^{b,i}, \qquad \text{on } C, \tag{7}$$

and

$$H_l^{b,s}(J_z) - H_l = -H_l^{b,i}, \qquad \text{on } C, \tag{8}$$

where C is the bounding contour of the cylinder and $\hat{l}$ is an unit vector tangential and counterclockwise along C . Equations (7) and (8) are the coupled equations for the unknown J_z and H_l . In these two equations, the scattered fields $E_z^{b,s}$ and $H_l^{b,s}$ are found to be [9]

$$\begin{aligned} E_z^{b,s}(\vec{\rho}) = & -\frac{k_b \eta_b}{4} \int_c J_z(\vec{\rho}') H_o^{(2)}(k_b|\vec{\rho} - \vec{\rho}'|) dl' \\ & + \frac{k_b \eta_b}{4\pi} \int_c J_z(\rho') \int_{-\infty}^{\infty} \Gamma_e(k_x) \frac{e^{j\beta_b(y+y')}}{\beta_b} e^{-jk_x(x-x')}\, dk_x dl', \end{aligned} \tag{9}$$

and

$$\begin{aligned} H_l^{b,s}(\vec{\rho}) = & \frac{J_z}{2} - \frac{jk_b}{4} \int_c (\rho') \cos\theta H_1^{(2)}(k_b|\vec{\rho} - \vec{\rho}'|) dl' \\ & - \frac{j}{4\pi} \int_c J_z(\vec{\rho}') \int_{-\infty}^{\infty} \frac{(\hat{n} \cdot \hat{x})(-jk_x) + (\hat{n} \cdot \hat{y})(j\beta_b)}{\beta_b} \cdot \\ & \Gamma_e(k_x) e^{j\beta_b(y-y')} e^{-jk_x(x-x')} dk_x dl', \end{aligned} \tag{10}$$

where $\vec{\rho}$ and $\vec{\rho}'$ are the position vector of field point and source point, and where

$$\Gamma_e(k_x) = \frac{\frac{\beta_a}{\mu_a} - \frac{\beta_b}{\mu_b}}{\frac{\beta_a}{\mu_a} + \frac{\beta_b}{\mu_b}} \quad , \tag{11a}$$

$$\beta_z = \sqrt{k_a^2 - k_x^2} \quad , \tag{11b}$$

$$\beta_b = \sqrt{k_b^2 - k_x^2} \quad , \tag{11c}$$

$$\cos\theta = \hat{n} \cdot \frac{(\vec{\rho} - \vec{\rho}')}{|\vec{\rho} - \vec{\rho}'|} \quad . \tag{11d}$$

In the above equations, k_a and k_b are the wavenumber, η_a and η_b are the wave impedance, in region a and b, respectively.

In Equations (7) and (8), the interior electric field $E_z^c(H_l)$ can be determined by solving the wave equation of the electric field in region c. Starting at Maxwell's equations, we derive a weak form of two-dimensional (2D) wave equation as

$$\begin{aligned} &\iint_A (\nabla \times \vec{E}^c) \times (\nabla \phi_m) \cdot \hat{z} ds - \iint_A k_c^2 \phi_m \vec{E}^c \cdot \hat{z} ds \\ &+ \iint_A \frac{1}{\mu_c} \phi_m (\nabla \times \vec{E}^c) \times \nabla \mu_c \cdot \hat{z} ds = \oint_C j\omega\mu_c \phi_m \vec{H}^c \cdot \hat{l} dl \, . \end{aligned} \tag{12}$$

One notes that when μ_C is a constant, as a special case of the general problem analyzed in this paper, Equation (12) reduces to the 2D version of Equation (23) given in [25]. Performing the vector calculations, we simplify Equation (12) to

$$\begin{aligned} \iint_A \nabla E_z^c \cdot \nabla \phi_m ds - \iint_A k_c^2 \phi_m E_z^c ds + \iint_A \frac{1}{\mu_c} \phi_m \nabla E_z^c \cdot \nabla \mu_c ds \\ = \oint_c j\omega\mu_c \phi_m H_l^c dl \, , \end{aligned} \tag{13}$$

which is the scalar weak form of wave equation for E_z^c.

In the analysis presented in this paper, TM plane wave illumination and the field due to an electric line source are admitted excitation. The incident fields $E_z^{b,i}$ and $H_l^{b,i}$ in Equations (7) and (8) are the z-component of electric field and the component of magnetic field tangential to the cylinder surface, respectively. Explicit expressions for

$E_z^{b,i}$ are given in [9]. $H_l^{b,i}$ can be computed by elementary method from the expressions of $E_z^{b,i}$.

3. Hybrid FEM/MOM Numerical Solution

The coupled Equations (7) and (8) are solved by a hybrid FEM/MOM numerical technique. First, we employ the pulse expansion & point matching MOM technique [32] to convert these two equations into a matrix form of linear equations. As depicted in Fig. 3, the cylinder bounding contour C is approximately represented by N_m straight-line segments, and the j^{th} segment is centered at l_j with length Δl_j, for $j = 1, 2, \cdots, N_m$.

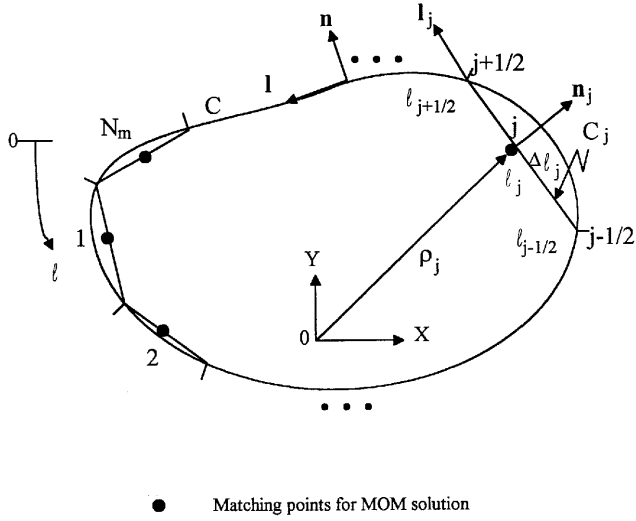

Figure 3. Partitioning of cylinder contour C into piecewise segments.

Then, the unknowns can be expanded as

$$J_z \approx \sum_{j=1}^{N_m} J_j \Pi_j(l) \tag{14a}$$

and

$$H_l \approx \sum_{j=1}^{N_m} H_j \Pi_j(l), \tag{14b}$$

in which $\Pi_j(l)$ is the pulse function [32] at the j^{th} segment. Using the pulse expansions given in (14a) and (14b) and point matching at centers of the line segments, we convert Equations (7) and (8) into a system of linear equations as

$$\sum_{j=1}^{N_m} J_j Z_{i,j}^b + \sum_{j=1}^{N_m} H_j Z_{i,j}^c = F_i, \tag{15}$$

and

$$\sum_{j=1}^{N_m} J_j Y_{i,j}^b + \sum_{j=1}^{N_m} H_j Z Y_{i,j}^c = G_i, \tag{16}$$

for $i = 1, 2, \cdots, N_m$. In Equations (15) and (16),

$$Z_{i,j}^b = E_z^{b,s}[l_i, \Pi_j(l')], \tag{17}$$
$$Z_{i,j}^c = -E_z^c[l_i, \Pi_j(l')], \tag{18}$$
$$Y_{i,j}^b = H_l^{b,s}[l_i, \Pi_j(l')], \tag{19}$$
$$Y_{i,j}^c = -\delta_{i,j}, \tag{20}$$
$$F_i = -E_z^{b,i}(l_i), \tag{21}$$
$$G_i = -H_l^{b,i}(l_i), \tag{22}$$

for $i = 1, 2, \ldots, N_m; j = 1, 2, \ldots, N_m$. In Equations (17)–(22), $E_z^{b,i}(l_i)$ and $H_l^{b,i}(l_i)$ are the known incident fields, $E_z^{b,s}[l_i, \Pi_j(l')]$, $E_z^c[l_i, \Pi_j(l')]$ and $H_l^{b,s}[l_i, \Pi_j(l')]$ are the fields produced by the pulse source $\Pi_j(l')$, all evaluated at the matching point l_i. In these equations, F_i and G_i can be found based on knowledge of the incident fields. $Z_{i,j}^b$ can be evaluated by using Equation (9) and expressed as

$$Z_{i,j}^b = Z_{i,j}^{b,1} + Z_{i,j}^{b,2}, \tag{23}$$

where

$$Z_{i,j}^{b,1} = -\frac{k_b \eta_b}{4} \int_{l_{j-\frac{1}{2}}}^{l_{j+\frac{1}{2}}} H_0^{(2)}(k_b |\vec{\rho}_i - \vec{\rho}_j - l' \vec{l}_j| dl', \tag{23a}$$

and

$$Z_{i,j}^{b,2} = \frac{k_b \eta_b}{4} \int_{l_{j-\frac{1}{2}}}^{l_{j+\frac{1}{2}}} \int_{-\infty}^{\infty} \Gamma_e(k_x) \frac{e^{j\beta_b[y_i + y_j + l'(l_j \cdot \hat{y})]}}{\beta_b} \cdot e^{-jk_x[x_i - x_j - l'(\hat{l}_j \cdot \hat{x})]} dk_x dl'. \tag{23b}$$

Similarly, $Y_{i,j}^b$ can be obtained by employing Equation (10) and expressed as

$$Y_{i,j}^b = Y_{i,j}^{b,1} + Y_{i,j}^{b,2}, \tag{24}$$

in which

$$Y_{i,j}^{b,1} = \frac{\delta_{i,j}}{2} - \frac{jk_b}{4} \int_{l_{j-\frac{1}{2}}}^{l_{j+\frac{1}{2}}} \cos\theta H_1^{(2)}(k_b|\vec{\rho}_i - \vec{\rho}_j - l'\vec{l}_j|) dl', \tag{24a}$$

and

$$Y_{i,j}^{b,2} = -\frac{j}{4\pi} \int_{l_{j-\frac{1}{2}}}^{l_{j+\frac{1}{2}}} \int_{-\infty}^{\infty} \frac{(\hat{n}_j \cdot \hat{x})(-jk_x) + (\hat{n}_j \cdot \hat{y})(j\beta_b)}{\beta_b} \Gamma_e(k_x) \cdot e^{j\beta_b[y_i + y_j + l'(\hat{l} \cdot \hat{y})]} e^{jk_x[x_i - x_j - l'(\hat{l} \cdot \hat{x})]} dk_x dl' \tag{24b}$$

One notes that Sommerfeld integrals are involved in $Z_{i,j}^{b,2}$ and $Y_{i,j}^{b,2}$. They are evaluated numerically in the same way as that presented in [9] and [10].

To solve Equations (15) and (16), it is also necessary to evaluate $Z_{i,j}^c$, which is related to the electric field $E_z^c[l_i, \Pi_j(l')]$ as given in Equation (18). $E_z^c[l_i, \Pi_j(l')]$ can be determined by an FEM solution of Equation (13). First, we divide the cylinder cross sectional area A into N_e triangle elements with N_n nodes and use A_e to denote the area of the e^{th} element, as shown in Fig. 4. Also depicted in Fig. 4 are N_m matching points used in the MOM solution procedure. Then, we expand the unknown E_z^c as

$$E_z^c = \sum_{n=1}^{N_n} E_n \phi_n(x, y) \qquad , \tag{25}$$

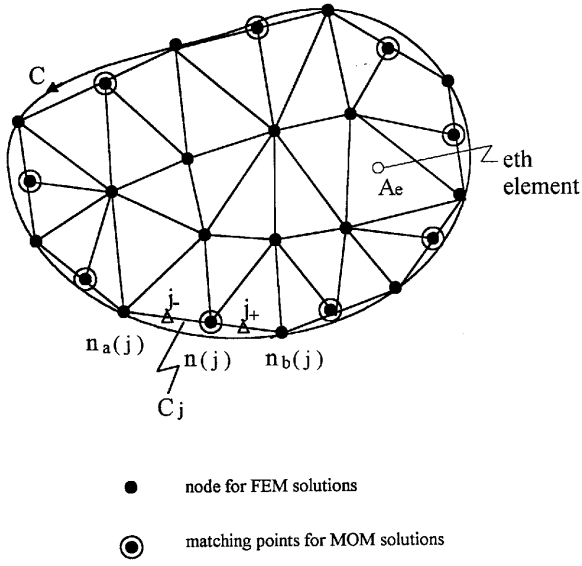

Figure 4. Subdivision of cylinder cross-sectional area A into triangular elements.

where $\phi_n(x, y)$ is the same as the weighting function $\phi_m(x, y)$ appearing in Equation (13), which is typically a locally supported polynomial. Substituting Equation (25) into (13), we have

$$\sum_{n+1}^{N_n} E_n \iint_A (\nabla\phi_m \cdot \nabla\phi_n - k_c^2\phi_m\phi_n + \frac{1}{\mu_c}\phi_m\nabla\phi_n \cdot \nabla\mu_c)ds = \oint_C j\omega\mu_c\phi_m H_l^c dl, \tag{26}$$

for $m = 1, 2, \cdots, N_n$. For convenience, Equation (26) is rewritten as

$$\sum_{n=1}^{N_n} E_n S_{m.n} = B_m(H_l) \quad , \tag{27}$$

for $m = 1, 2, \cdots, N_n$, or in matrix form

$$[S][E] = [B(H_l)] \quad , \tag{27'}$$

in which the coefficient matrix element $S_{m,n}$ and the forcing vector element $B_m(H_l)$ can be found by

$$S_{m,n} = \iint_A (\nabla\phi_m \cdot \nabla\phi_n - k_c^2 \phi_m \phi_n + \frac{1}{\mu_c}\phi_m \nabla\phi_n \cdot \nabla\mu_c) ds, \qquad (27a)$$

and

$$B_m(H_l) = \oint_C j\omega\mu_c \phi_m H_l^c dl \qquad , \qquad (27b)$$

for $m = 1, 2, \cdots N_n$. One notes that the global matrix element $S_{m,n}$ involves an integration over the entire region A. Instead of determining $S_{m,n}$ directly, we first calculate the corresponding local matrix element $S_{k,l}^e$ which can be found by an integration over the e^{th} element as

$$S_{k,l}^e = S_{k,l}^{e,1} + S_{k,l}^{e,2} \qquad , \qquad (28)$$

where

$$S_{k,l}^{e,1} = \iint_{A_e} (\nabla\alpha_k \cdot \nabla\alpha_l - k_c^2 \alpha_k \alpha_l) ds \qquad , \qquad (28a)$$

and

$$S_{k,l}^{e,2} = \iint_{A_e} (\frac{1}{\mu_c}\alpha_k \nabla\alpha_l \cdot \nabla\mu_c) ds \qquad , \qquad (28b)$$

for $e = 1, 2, \cdots, N_e$, $k = 1, 2, 3$, and $l = 1, 2, 3$. In the above equations, the interpolation function $\alpha_l(x, y)$ is defined in [33]. Using a basic formula given in [33,34], we rewrite Equations (28a) and (28b) as

$$S_{k,l}^{e,1} = \frac{1}{4\Delta^e}(b_k^e b_l^e + c_k^e c_l^e) - (k_c^e)^2 \frac{\Delta^e}{12}(1 + \delta_{i,j}) \qquad , \qquad (29a)$$

and

$$S_{k,l}^{e,2} = \frac{1}{\mu_c^e}\frac{1}{6}(b_l^e \frac{\partial\mu_c^e}{\partial x} + c_l^e \frac{\partial\mu_c^e}{\partial y}) \qquad , \qquad (29b)$$

for $e = 1, 2, \cdots, N_e$; $k = 1, 2, 3$; and $l = 1, 2, 3$. In Equations (29a) and (29b), $\delta_{i,j}$ is the Derac delta function defined by

$$\delta_{i,j} = \begin{cases} 1, & i = j \\ 0, & i \neq j \end{cases} \qquad (30)$$

μ_c^e, k_c^e, $\partial\mu_c^e/\partial x$, and $\partial\mu_c^e/\partial y$ represent the corresponding average values in the e^{th} element and are taken to be the values evaluated at

the center of the element. After obtaining the local matrix elements $S^e_{k,l}$, the global matrix elements $S_{m,n}$ can be found by a process of assembly, which is a selective summation of the related local matrix elements. The details of the assembly procedure is given in [33,35]. The forcing vector element $B_m(H_l)$ appearing in Equation (27), corresponding to the j_{th} pulse source $\Pi_j(l)$ defined in (18) as H_l, can be found by Equation (27b) as

$$B^j_m(H_l) = j\omega \int_{C_j} \mu_c \phi_m dl \qquad , \tag{31}$$

where C_j is the j^{th} straight-line segment depicted in Fig. 3. An analytical integration of Equation (31) results in

$$B^j_m(H_l) = \begin{cases} j\omega\mu_c^{j-}\Delta l_j/4, & m = n_a(j) \\ j\omega(\mu_c^{j-} + \mu_c^{j+})\Delta l_j/4, & m = n(j) \\ j\omega\mu_c^{j+}\Delta l_j/4, & m = n_b(j) \\ 0, & \text{otherwise,} \end{cases} \tag{32}$$

where $n(j)$ is the index of the node coinciding with the j^{th} matching point, $n_a(j)$ and $n_b(j)$ are indices of the nodes right behind and immediately in front of the j^{th} matching point in a counter-clockwise sense on the bounding contour C, as shown in Fig. 4. In Equation (32), μ^{j-} and μ^{j+} are the permeability at the center points of the segments $[n_a(j), n(j)]$ and $[n(j), n_b(j)]$. These point are also depicted in Fig. 4.

The numerical technique developed above can be used for the analysis of an inhomogeneous cylinder, μ_c and ε_c of which may be continuous, piecewise continuous, or discrete functions of position. For the case that μ_c and ε_c are piecewise continuous or discrete functions of position, the cylinder cross section is divided in such a way that the permeability and the permittivity of the material are either continuous or constants within each element. To solve Equation (27') for the electric field, we use a matrix inversion and multiplication procedure, and rewrite the equation as

$$[E] = [S]^{-1}[B(H_l)] \qquad . \tag{33}$$

One notices that the solution of Equations (15) and (16) requires knowledge of the electric field $E^c_z[l_i, \Pi_j(l')]$ due to the pulse source

$\Pi_j(l')$. Therefore, we substitute $B_m^j(H_l)$ corresponding to the j^{th} pulse source $\Pi_j(l)$, given in Equation (31), in place of $B(H_l)$ in (33) and arrive at

$$[E_n] = [S]^{-1}[B_m^j(H_l)] \qquad , \tag{34}$$

for $n = 1, 2, \cdots, N_n$. One notes that the coefficient matrix [S] is independent from the excitation H_l. Therefore, we only need to find the inverse of the matrix [S] once. Solving Equation (34) and collecting the solutions of E_n at the nodes $n = n(i)$, which coincide with the i^{th} matching points encountered in the MOM solution scheme, we can obtain the j^{th} column elements of $[Z_{i,j}^c]$ defined in Equation (18) as

$$Z_{i,j}^c = -E_{n(i)} \qquad , \tag{35}$$

for $i = 1, 2, \cdots, N_m$. Repeating this procedure for all the pulse sources $\Pi_j(l')$, we get numerical solutions of the matrix elements $Z_{i,j}^c$ for $i = 1, 2, \cdots, N_m$, $j = 1, 2, \cdots, N_m$. The results of $Z_{i,j}^c$, then, can be substituted back to Equations (15) and (16), for the numerical solution of the unknown J_j and H_j. The solution of Equations (15) and (16) requires N_m FEM solutions corresponding to N_m excitation functions $B_m^j(H_l)$. However, since the coefficient matrix [S] for the FEM solution is independent from the excitation function $B_m^j(H_l)$, we only need to invert the matrix [S] once.

4. Far-Zone Scattered Field and Field Inside the Cylinder

After solving Equations (15) and (16), the numerical results of the equivalent electric surface current J_z can be used to compute the far-zone scattered electric field by

$$E_z^a = \oint_C J_z(\vec{\rho}')e_z^{ab}(\vec{\rho}, \vec{\rho}')dl' \qquad , \tag{36a}$$

in region a and

$$E_z^b = \oint_C J_z(\vec{\rho}')e_z^{bb}(\vec{\rho}, \vec{\rho}')dl' \qquad , \tag{36b}$$

in region b. In the above equations, $J_z(\vec{\rho}')$ can be replaced by its pulse expansion of Equation (14a), leading to

$$E_z^a = \sum_{j=1}^{N_m} J_j \int_{C_j} e_z^{ab}(\vec{\rho}, \vec{\rho}')dl' \quad , \tag{37a}$$

and

$$E_z^b = \sum_{j=1}^{N_m} J_j \int_{C_j} e_z^{bb}(\vec{\rho}, \vec{\rho}')dl' \quad , \tag{37b}$$

where $e_z^{ab}(\vec{\rho}, \vec{\rho}')$ and $e_z^{bb}(\vec{\rho}, \vec{\rho}')$ are given in Equations (18a) and (18b) of [11].

Also, after solving Equations (15) and (16), the numerical results of H_j can be used for determining the tangential magnetic field H_l on the bounding contour C by substituting H_j into Equation (14b). Meanwhile, based on information of H_j, the electric field inside the cylinder can be determined by solving Equation (33) in which the forcing vector element can be found by

$$B_m(H_l) = \sum_{j=1}^{N_m} H_j B_m^j(H_l) \quad , \tag{38}$$

where $B_m^j(H_l)$ is given in Equation (32).

5. Results and Discussion

In this section are presented numerical results for the equivalent current distributed on, and the far-zone electric field scattered by a buried inhomogeneous cylinder under TM excitation. Selected data of the total electric field inside the cylinder are also given. Even though the numerical technique presented in this paper is suitable for the analysis of a buried inhomogeneous cylinder of general cross section, only the data for a rectangular cylinder, chosen as an example, are shown. As illustrated in Fig. 5, L and W denote the length and width of the rectangular cylinder, D stands for the buried depth of the cylinder, which is measured from the interface between the two half-spaces to the symmetry axis of the cylinder cross section. The upper half space

is taken to be free space ($\mu_a = \mu_o$, $\varepsilon_a = \varepsilon_o$), the lower half space is assumed to be lossless and the permeabilities of both regions are assumed to be the same ($\mu_a = \mu_b = \mu_o$). The medium in region c (the region inside the cylinder) is taken to be a lossy material with permittivity ε_c , conductivity σ_c , and permeability μ_c . The medium c parameters may be either continuous or discrete functions of the position within the cylinder. As examples of inhomogeneity of the cylinder, two cases are considered and illustrated in Fig. 5: a continuous variation of ε_c and μ_c ; and four homogeneous layers characterized by ($\mu_{c,i}$, $\varepsilon_{c,i}$); both with a constant conductivity σ_c . The operating frequency is chosen to be 300 MHz for all the data presented. The equivalent electric current J_z is normalized to $H_x^{b,i}$, the x-component of the incident magnetic field evaluated at the origin. The total electric field inside the cylinder E_z^c is normalized to $E_z^{b,i}$, the incident electric field, also evaluated at the origin.

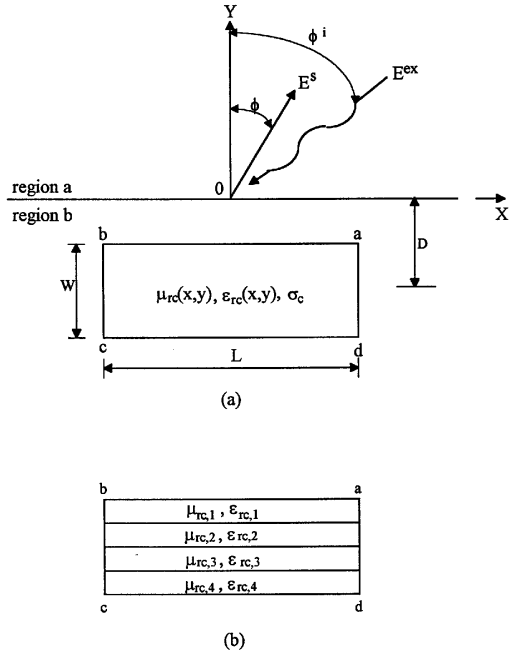

Figure 5. Cross section of a buried rectangular cylinder. (a) Continuous permittivity and permeability distribution; (b) Four-layer structure with discrete permittivity and permeability distribution.

The convergence of the numerical results has been tested in the computation. To check the accuracy of the hybrid integral and differential equation method (HM) presented, we first compare the HM results with the corresponding surface integral equation (SIE) solutions [17] for a buried homogeneous cylinder which can be considered as a special case of inhomogeneous cylinders. In Fig. 6 is shown the comparison of the equivalent currents in magnitude and phase, as well as the far-zone scattered field patterns. One observes that the HM results and HIE solutions of the magnitude (depicted in Fig. 6(a)) and the phase (shown in Fig. 6(b)) of the normalized currents are very close, and the far-zone field patterns (illustrated in Fig. 6 (c)) obtained by these two methods fall on top of each other. Then, we compare the HM solutions with the corresponding hybrid integral equation (HIE) results [21] for a buried inhomogeneous cylinder with continuous permittivity and permeability. In Fig. 7 is shown the comparison of the far-zone scattered field patterns for a buried cylinder whose relative permittivity varies as $\varepsilon_{rc} = [2 + 2\cos(\pi x/L)][2 + 2\cos(\pi(y + D)/W)]$. A good agreement is observed.

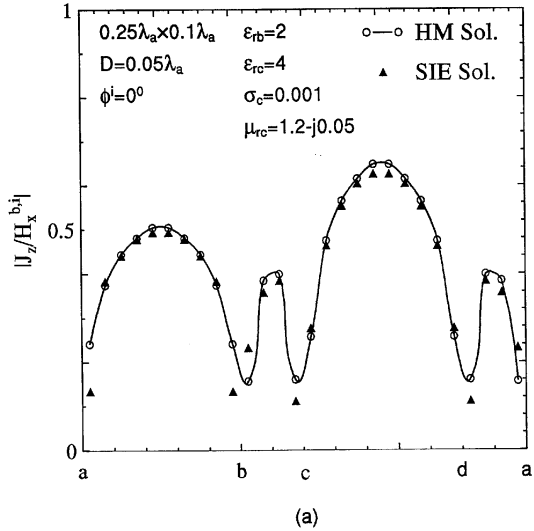

Figure 6. Comparison of hybrid integral and differential equation method (HM) solutions and surface integral equation (SIE) solutions for a buried homogeneous rectangular cylinder subject to normally incident TM plane wave illumination. (a) Magnitude of normalized equivalent current.

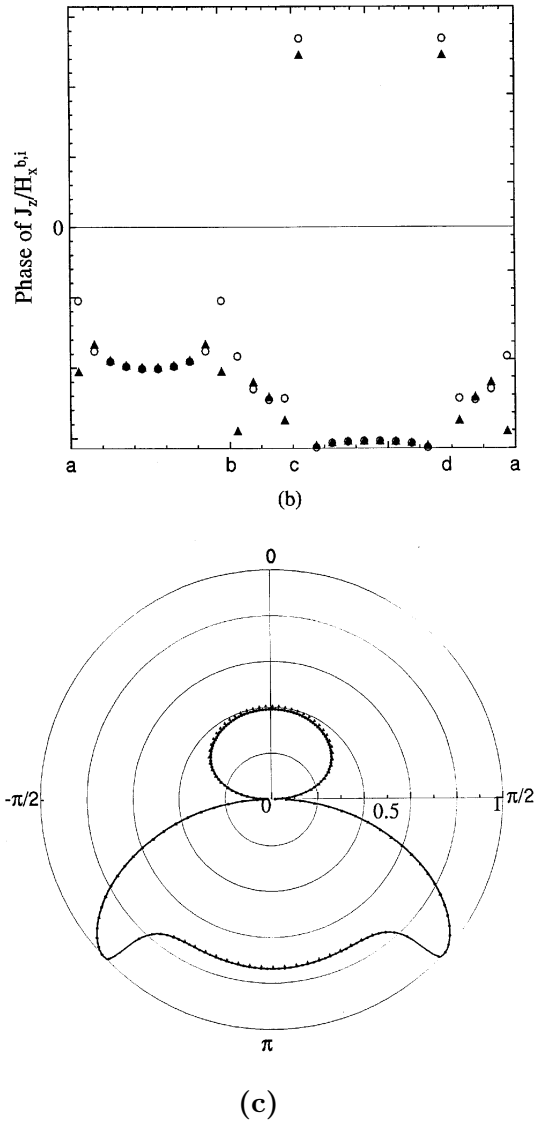

(c)

Figure 6. Comparison of hybrid integral and differential equation method (HM) solutions and surface integral equation (SIE) solutions for a buried homogeneous rectangular cylinder subject to normally incident TM plane wave illumination. (b) Phase of normalized equivalent current; (c) Far-zone field pattern.

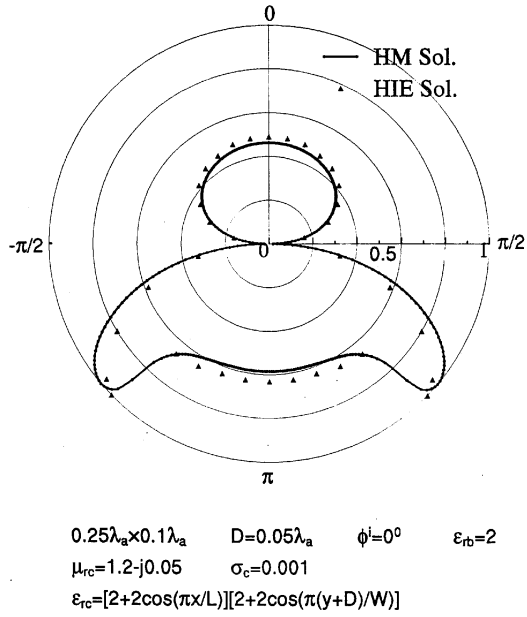

Figure 7. Comparison of hybrid integral and differential equation method (HM) solutions and hybrid integral equation (HIE) solutions for a buried inhomogeneous rectangular cylinder subject to normally incident TM plane wave illumination: far-zone field pattern.

In Fig.8 are shown the far-zone field patterns for a buried rectangular cylinder with a constant permittivity and continuously-varying permeabilities. One notes that the field patterns are of similar shape for all three different permeability variations, but the field intensity becomes stronger as the coefficient of the square variation term of the permeability gets larger. This is because that the larger this coefficient is, the larger the average values of the relative permeability of the cylinder becomes, which results in stronger scattered field. In addition, one notes that the field pattern for $\mu_{rc} = (1.2 - j0.05)[1 + 0.5(2x/L)^2][1 + 0.5(2(y + D)/W)^2]$ in Fig. 8 is asymmetrical about y-axis. This is due to the fact that the equivalent surface current distribution depends on both the permeability and its derivative, and the latter is not symmetrical about y-axis. Data depicted in Fig. 9 illustrate the influence of different permittivities of the medium in region b on the far-zone

scattered field pattern. A significant change of the field patterns can be observed for different ε_{rb}. And as ε_{rb} increases, the strength of the scattered field decreases as one would expect. In Fig. 10 are depicted the far-zone scattered field patterns for different buried depth of the cylinder. It can be seen, from this figure, that the strength of the scattered field does not change significantly with the buried depth since the magnitude of the excitation field does not vary with buried depth. But it can also been seen that for deeper-buried cylinder, the scattered field pattern has multiple lobes in region b and the main lobe tends to be oriented towards the horizontal axis.

In Figs. 11–13 are presented magnitudes of the normalized electric fields inside a buried rectangular cylinder, with a continuously-varying permittivity (Fig. 11); of four-layer structure with a discrete permittivity distribution (Fig. 12); of four-layer structure with a discrete permeability distribution (Fig. 13). Continuous electric field distributions inside the cylinder are observed for all of these three cases including those with discontinuous electromagnetic parameters. This is expected because the electric field is z-directed and it is tangential to the interfaces of the four layers of the cylinder

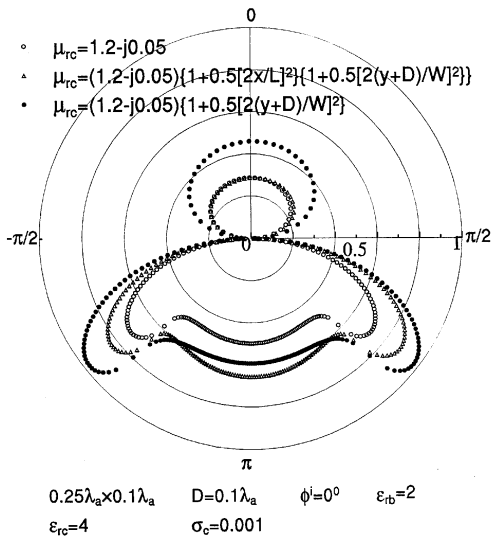

Figure 8. Far-Zone field pattern for a buried inhomogeneous rectangular cylinder subject to normally incident TM plane wave illumination, for different relative permeability μ_{rc} variations.

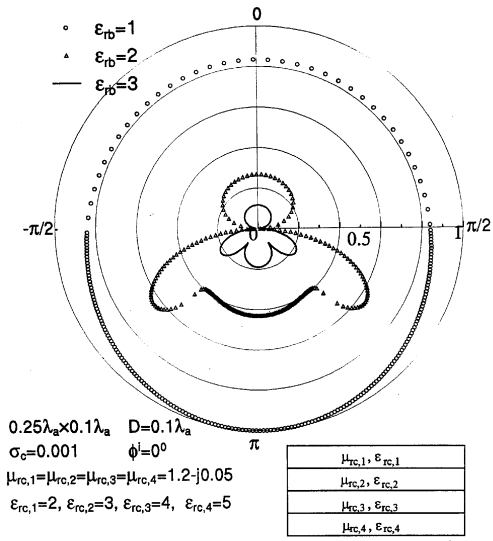

Figure 9. Far-Zone field pattern for a buried inhomogeneous rectangular cylinder of four-layer structure, subject to normally incident TM plane wave illumination, for different region b permittivities.

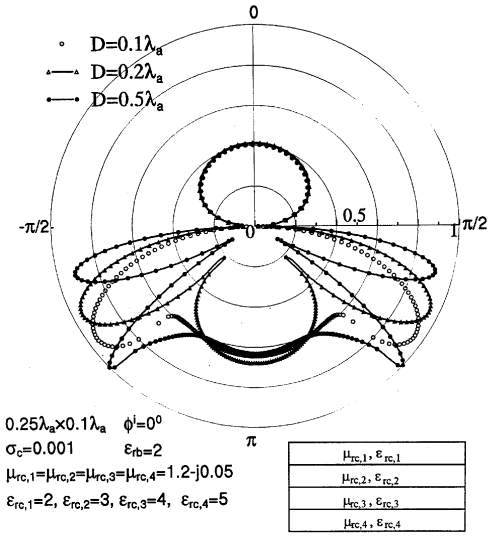

Figure 10. Far-Zone field pattern for a buried inhomogeneous rectangular cylinder of four-layer structure, subject to normally incident TM plane wave illumination, for different buried depth.

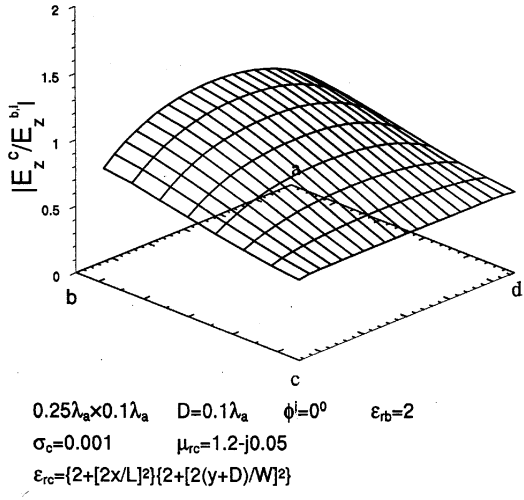

Figure 11. Magnitude of normalized total electric field inside a buried inhomogeneous rectangular cylinder with a continuous relative permittivity ε_{rc}, subject to normally incident TM plane wave illumination.

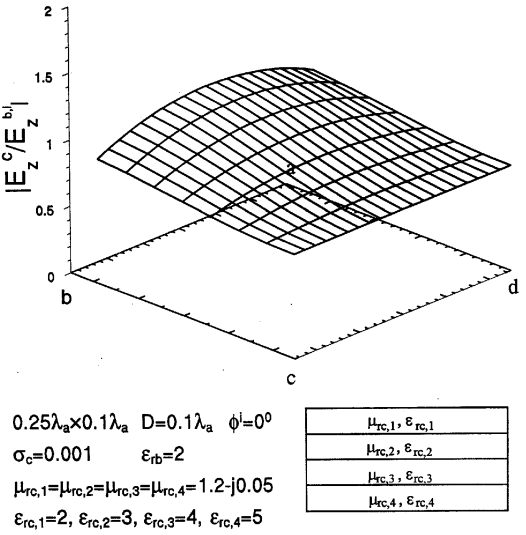

Figure 12. Magnitude of normalized total electric field inside a buried inhomogeneous rectangular cylinder of four-layer structure with discrete permittivity distribution $\varepsilon_{cr,i}$, subject to normally incident TM plane wave illumination.

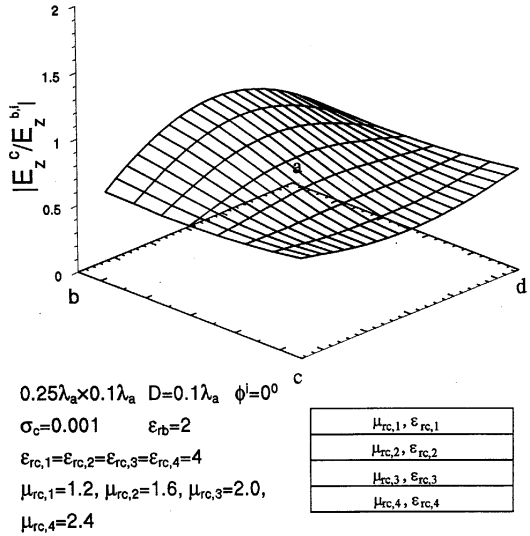

Figure 13. Magnitude of normalized total electric field inside a buried inhomogeneous rectangular cylinder of four-layer structure with discrete permeability distribution $\mu_{cr,i}$, subject to normally incident TM plane wave illumination.

References

1. D'Yakonov, B. P., "The diffraction of electromagnetic waves by a circular cylinder in a homogeneous half space," *Bull. Acad. Sci. U.S.S.R. Geophysics*, Vol. 9, No. 1/2, 950–995, 1959.
2. Howard, A. Q., "The electromagnetic fields of a subterranean cylindrical inhomogeneity excited by a line source," *Geophysics*, Vol. 37, 975–984, Dec. 1972.
3. Hohmann, G. W., "Electromagnetic scattering by conductors in the earth near a line source of current," *Geophysics*, Vol. 36, 101–131, Feb. 1971.
4. Parry, H. R., and S. H. Ward "Electromagnetic scattering from cylinders of arbitrary cross-section in a conductive half-space," *Geophyscis*, Vol. 36, 67–100, Feb. 1971.
5. Wait, J. R., "The cylindrical Ore body in the presence of a cable carrying an oscillating current," Geophysics, Vol. 17, 378–386, April 1952.

6. Wait, J. R., "The effect of a buried conductor on the subsurface fields for line source excitation," *Radio Science*,Vol. 7, 587–591, May 1972.
7. Mahmoud, S. F., S. M. Ali, and J. R. Wait, "Electromagnetic scattering from a buried inhomogeneity inside a lossy earth," *Radio Science*, Vol. 16, 1285–1298, Nov.–Dec. 1981.
8. Butler, C. M., "Current induced on a conducting strip which resides on the planar interface between two semi-infinite half-spaces," *IEEE Trans. Antennas propagat.*, Vol. AP-33, 226–231, March 1984.
9. Butler, C. M., X.-B. Xu, and A. W. Glisson, "Current induced on a conducting cylinder located near the planar interface between two semi-Infinite half-spaces," *IEEE Trans. Antennas propagat.*, Vol. AP-33, 616–624, June 1985.
10. Turner, C. D., and L. D. Bacon, "Evaluation of a thin-slot formalism for finite-difference time-domain electromagnetic codes," *IEEE Trans. Elect. Compat.*, Vol. 30, 523–528, Nov. 1988.
11. Xu, X.-B., and C. M. Butler, "Scattering of TM excitation by coupled and partially buried cylinders at the interface between two media," *IEEE Trans. Antennas propagat.*, Vol. AP-35, 529–538, May 1987.
12. Xu, X.-B., and C. M. Butler, "Scattering of TE excitation by partially buried and coupled strips near a planar media interface," *J. Electromag. Waves Applic.,* Vol. 4, No. 8, 727–742, 1990.
13. Xu, X.-B., and C. M. Butler, "Current induced by TE excitation on coupled and partially buried bylinders at the interface between two media," *IEEE Trans. Antennas propagat.*, Vol. AP-38, 1823–1828, Nov. 1990.
14. Butler, C. M., and X.-B. Xu, "TE scattering by partially and coupled cylinders at the interface between two media," *IEEE Trans. Antennas propagat.*,Vol. AP-38, 1829–1934, Nov. 1990.
15. Michalski, K. A., and D. Zheng, "Electromagnetic scattering and radiation by surfaces of arbitrary shape in layered media, Part I: theory," *IEEE Trans. Antennas propagat.*, Vol. AP-38, 335–344, March 1990.
16. Michalski, K. A., and D. Zheng, "Electromagnetic scattering and radiation by surfaces of arbitrary shape in layered media, Part II: implementation and results for contiguous half-space" *IEEE Trans. Antennas propagat.*, Vol. AP-38, 345–352, March 1990.

17. Butler, C. M., and X.-B. Xu, "Scattering by a lossy dielectric cylinder buried below the planar interface between two semi-infinite half spaces," *Meeting Digest, 1989 National Radio Science Meeting*, San Jose, CA, June 1989.
18. Diamandi, I., and J. N. Sahalos, "Frequency and time domain analysis of the scattered field of buried dielectric targets," *Archiv fur Electrotechnik*, Vol. 77, 441–449, Sept. 1991.
19. Izadian, J. L., L. Peters, Jr., and J. H. Richmond, "Computation of scattering from penetrable cylinders with improved numerical efficiency," *IEEE Trans. Geosci. Remote Sensing*, Vol. GE-22, 52–61, Jan. 1984.
20. Jin, J. M., V. V. Liepa, and C. T. Tai, "A volume-surface integral equation for electromagnetic scattering by inhomogeneous cylinders," *J. Electromagn. Waves Applic.*, Vol. 2, No. 5/6, 573–588, 1988.
21. Eggimann, W. H., "Higher-order evaluation of electromagnetic diffraction by circular disks," *IEEE Trans. Microwave Theory and Tech.*, 408–418, Sept. 1961.
22. Xu, X.-B., and W. Yan, "Scattering of TM excitation by inhomogeneous cylinders near a media interface - a hybrid integral equation approach," *J. Electromagn. Waves Applic.*, Vol. 7, Vol. No. 7, 919–941, 1993.
23. Xu, X.-B., and W. Yan, "Modification of hybrid integral equations for determining scattering by an inhomogeneous cylinder of discontinous electromagnetic parameters near a media interface," *J. Electromagn. Waves Applic.*, Vol. 7, No. 10, 1389–1393, 1993.
24. Pearson, L. W., and A. F. Peterson, et al., "Inward-looking and outward-looking formulation for scattering from penetrable objects," *IEEE Trans. Antennas propagat.*, Vol. AP-40, 714–720, June 1992.
25. Yuan, X., D. R. Lynch, and J. W. Strohbehn, "Coupling of finite element and moment methods for electromagnetic scattering from inhomogeneous objects," *IEEE Trans. Antennas propagat.*, Vol. AP-38, 386–393, March 1990.
26. Lynch, D. R., K. D. Paulson, and J. W. Strohbehn, "Finite element solution of Maxwell's equation for hypothermia treatment planning," *J. Computational Physics*, Vol. 58, 246–269, 1985.

27. Antilla, G. E., and N. G. Alexopoulos, "Scattering from complex three-dimensional geometries by a curvilinear hybrid finite element integral equation approach," *Journal of the Optical Society of America A.*, Vol. 11, No. 4, 1445–1457, April 1994.
28. errata to [26], JOSA-A, Dec. 1994.
29. Antilla, G. E., "Radiation and scattering from complex 3D geometries using a curvilinear hybrid finite element integral equation approach," Ph.D. dissertation, University of California, Los Angeles, CA, 1993.
30. Sommerfeld, A., *Partial Differential Equations*, New York, Academic Press, 1949.
31. Harrington, R. F., *Time-Harmonic Electromagnetic Fields*, New York, McGraw-Hill, 1961.
32. Harrington, R. F., *Field Computation by Moment Methods*, New York, Macmillan, 1968.
33. Jin, J., *The Finite Element Method in Electromagnetics*, New York, John Wiley and Sons, Inc., 1993.
34. Silvester, P. P., *Finite Elements for Electrical Engineers*, Cambridge England: Cambridge University press, 1990.
35. Ao, J., "A hybrid integral and differential equation method for scattering from a buried inhomogeneous cylinder under TM excitation," Master's Thesis, Clemson University, Clemson, SC, May 1995.